Extending EDMF into the statistical modeling of boundary layer clouds

Roel A. J. Neggers

ECMWF, Shinfield Park, Reading
RG2 9AX, United Kingdom
Roel.Neggers@ecmwf.int

1 Introduction

The representation of clouds in general circulation models (GCM) is still causing significant uncertainty in numerical climate and weather prediction, through the associated strong impact on the earth's radiative budget (Intergovernmental Panel on Climate Change (IPCC) Third Assessment Report; Houghton 2001). The same is true for turbulent transport in the boundary layer, which controls the exchange of moist static energy and momentum between the surface and the free troposphere. As both clouds and turbulence are sub-grid processes their impact has to parameterized, which has been the subject of active research. Typically, transport and clouds are represented in separate schemes in GCMs. This separation potentially introduces compensating errors, masked by the tuning of adjustable parameters. These errors can be avoided by unification and integration of separate schemes, which for that reason has been a recent trend in atmospheric modelling (e.g. Lappen and Randall 2001; Golaz 2002).

This study relates a similar attempt at sub-grid model integration. It presents the extension of the Eddy Diffusivity Mass Flux (EDMF) framework for turbulent transport (Siebesma and Teixeira 2000) into the statistical modeling of boundary layer clouds (e.g. Sommeria and Deardorff 1977; Mellor 1977; Bougeault 1981). Such close coupling between the modeling of boundary layer transport and clouds is motivated by the idea that both are in principle generated by the same turbulent eddies. The associated eddy sizes and turn-over timescales are relatively small compared to the typical timestep and gridspacing of present-day weather prediction and climate models, which favours a statistical modeling approach.

The integration of the representation of clouds and transport is achieved by parameterizing both as a function of the same joint-distribution, reconstructed using EDMF transport model variables. As a result, the representation of transport and clouds becomes internally consistent within the boundary layer scheme. Projection of the advection-diffusion decomposition that defines EDMF on the turbulent distribution implies that each transport component gets its own independent probability density function (PDF), resulting in a diffusive PDF and an updraft PDF. This corresponds to a bimodal cloud scheme (Lewellen and Yoh 1993). An attractive aspect of such bimodal models is that they can theoretically render distributions with high (in principle unlimited) skewness and kurtosis. Such distributions are typical of convective layers, in which the updrafts are often grouped and form an independent, second mode.

Compared to previous statistical cloud schemes this approach has some novelties. First, the double PDF is reconstructed in conserved variable space, the position and orientation of each PDF expressing its unique properties. Second, the parameterization of the variances of the double PDF introduces close ties to the transport model. The gridbox mean variance is reconstructed using a prognostic budget including a variance transport term. The variance of the updraft PDF is parameterized as a function of the spread among multiple resolved model updrafts, introduced into EDMF by Neggers et al. (2007) to enable representation of shallow cumulus

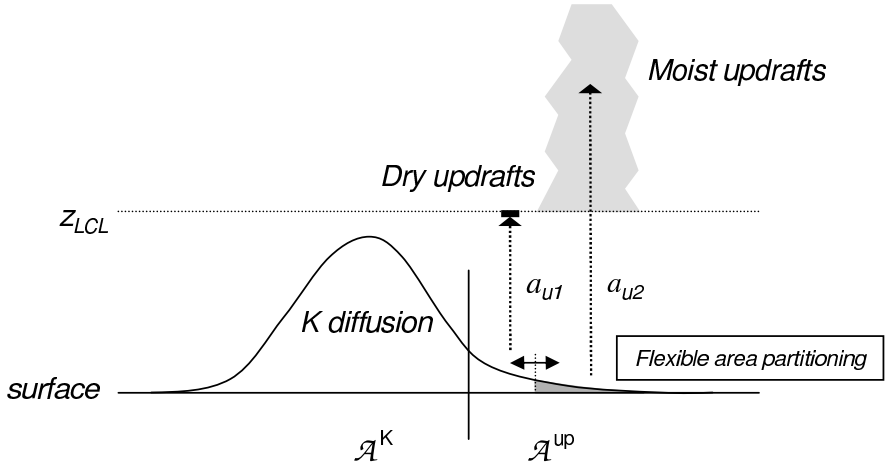

Figure 1: The eddy diffusivity mass flux (EDMF) framework for boundary layer convection, featuring multiple updrafts. $\mathscr{A}^{up}$ is the fraction explicitly represented by advective updrafts, while $\mathscr{A}^{K}$ represents diffusive motions. Fraction a_{u1} represents dry updrafts that never reach their lifting condensation level, while fraction a_{u2} represents updrafts that condense and become positively buoyant cumulus clouds (shaded grey).

convection. Finally, for the integration of cloud fraction and condensate on these PDFs the common method applied in previous single-Gaussian models (Sommeria and Deardorff 1977; Mellor 1977) is used, except that it is now applied to a *double* PDF, making use of vector notation throughout the formulation to facilitate this procedure.

The technique is implemented into the ECMWF planetary boundary layer (PBL) scheme and evaluated against large-eddy simulation (LES) results. Section 2 shortly describes the EDMF framework featuring multiple updrafts. Section 3 describes its extension into the statistical modeling of boundary layer clouds and precipitation. Section 4 presents an evaluation of the scheme against some prototype Trade-wind cloudy PBL scenarios, which are then further discussed in section 5.

2 The eddy diffusivity mass flux (EDMF) framework

The eddy diffusivity mass flux (EDMF) framework was formulated by Siebesma and Teixeira (2000) and Siebesma et al. (2007). While small perturbations tend to do transport in a more diffusive manner (down-gradient), organized updrafts are able to overcome local stability and hence do transport against local gradients. This has been the motivation for representing counter-gradient transport terms alongside pure diffusive, K-diffusion terms (Holtslag and Moeng 1991). Motivated by these arguments a decomposition is made of the total turbulent flux $\overline{w'\phi'}$ of conserved state variables $\phi \in \{q_t, \theta_l\}$ into an advective part by organized updrafts and a diffusive part by weaker, more random perturbations,

$$\overline{w'\phi'} = \mathscr{A}^{\mathrm{up}}\,\overline{w'\phi'}^{\mathrm{up}} + \mathscr{A}^{\mathrm{K}}\,\overline{w'\phi'}^{\mathrm{K}} \tag{1}$$

where $\mathscr{A}^{\mathrm{up}}$ is the area fraction covered by the organized updrafts, and $\mathscr{A}^{\mathrm{K}} = 1 - \mathscr{A}^{\mathrm{up}}$ is that covered by the remaining, "diffusive" air. Based on the typically observed small values of the area fraction covered by organized updrafts we choose the value $\mathscr{A}^{\mathrm{up}} = 0.1$. The vertical transport by the smaller turbulent perturbations

is represented by a down-gradient diffusive term,

$$\mathscr{A}^{\mathrm{K}}\,\overline{w'\phi'}^{\mathrm{K}} \;=\; -K_{\phi}\,\frac{\partial\overline{\phi}}{\partial z}. \tag{2}$$

The advective transport by organized updrafts is explicitly modeled using an ensemble mass flux model,

$$\mathscr{A}^{\mathrm{up}}\,\overline{w'\phi'}^{\mathrm{up}} \;=\; \sum_{i=1}^{I} M_{ui}\,\left(\phi_{ui}-\overline{\phi}\right), \tag{3}$$

where subscript u indicates the property of a specific updraft group with i is its index number, and I is the total number of such updraft groups. $M_{ui} \equiv a_{ui}\,w_{ui}$ is the collective volumetric mass flux of group i, with a_{ui} the area fraction covered by all updrafts in group i ($\mathscr{A}^{\mathrm{up}} = \sum_{i=1}^{I} a_{ui}$) and w_{ui} the collective vertical velocity of group i. The properties of each group are obtained from a rising plume budget model.

Implementation of the EDMF scheme into the ECMWF Integrated Forecasting System (IFS) is documented by Köhler (2005) and Tompkins et al. (2004). It is yet only applied to the well-mixed PBL, including dry convection and stratocumulus convection. Recently, the number of resolved updrafts was expanded from one to two, to allow the EDMF framework to represent conditionally unstable cloud layers such as found in the shallow cumulus topped PBL. In this dual mass flux framework (DualM), a dry mixed-layer updraft and moist cumulus updraft can coexist. Their area partitioning is made flexible, to allow representation of moist convective inhibition mechanisms through the moist updraft area fraction. Also included are stability feedbacks on the vertical structure of cloudy mass flux, and an entrainment efficiency closure at PBL top (Wyant et al. 1997). The DualM transport scheme is described in full detail by Neggers et al. (2007). Figure 1 shows a schematic overview of the EDMF scheme featuring multiple updraft groups.

3 Extension into the statistical cloud scheme

The advection-diffusion decomposition is now projected onto the distribution that is used in the statistical cloud scheme. This implies that each EDMF component gets its own independent PDF, resulting in an updraft PDF and a diffusive PDF. Such partitioning is characteristic of observed distributions in convective situations, in which the updrafts are often grouped and form a distinct separate mode (e.g. Larson et al. 2001). Unimodal PDF schemes can never reproduce the potential impacts of such independent updraft modes on cloud fraction and condensate. Figure 2a contains an example from LES BOMEX, showing the organization into a weakly buoyant "passive" PDF and a second, positively buoyant updraft PDF.

3.1 Orientation in conserved variable space

The bimodal cloud scheme is constructed in conserved variable space, as schematically illustrated in Fig. 2b. The EDMF partitioning (1) is applied to the total PDF G, resulting in an updraft PDF G^{up} and a diffusive PDF G^{K}.

$$G \;=\; \mathscr{A}^{\mathrm{up}}\,G^{\mathrm{up}} \;+\; \mathscr{A}^{\mathrm{K}}\,G^{\mathrm{K}} \tag{4}$$

Both PDFs are assumed to be Gaussian, shown by Lewellen and Yoh (1993) to give representative distributions in convective situations. These PDFs are parameterized as a function of transport model variables, ensuring a close coupling between clouds and transport. For example, using vector notation $\mathbf{\Phi} = (q_t, \theta_l)$, the means of the updraft and diffusive PDF are $\overline{\mathbf{\Phi}}^{\mathrm{up}}$ and $\overline{\mathbf{\Phi}}^{\mathrm{K}}$ respectively. The linear axes of the joint-PDFs are defined by a unit vector $\hat{v}$, their orientation reflecting the unique character of each PDF; the updraft-PDF axis $\hat{v}^{\mathrm{up}}$ is positioned

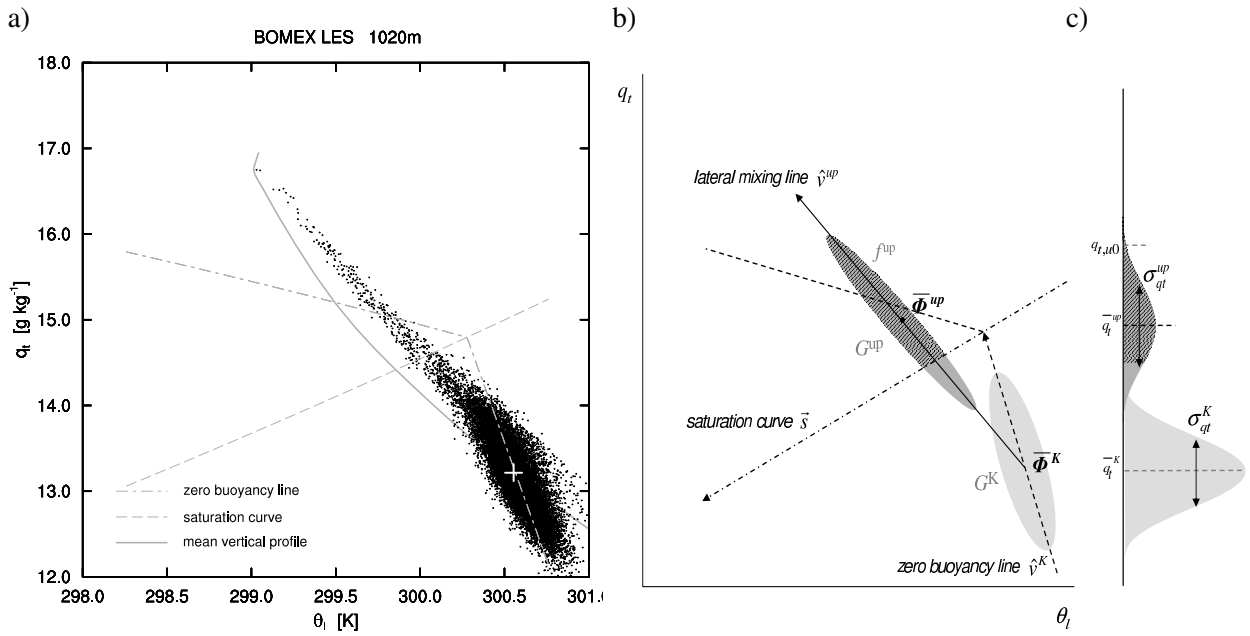

Figure 2: a) LES scatterplot of specific humidity and potential temperature at 1020*m during BOMEX. The grey lines represent the mean vertical profile (solid, with the white cross indicating the value at this height), the saturation curve (dashed) and the zero-buoyancy line (dash-dotted). b) The rendering of this distribution by the vectorized bimodal framework, including the orientation of the PDF axes $\hat{v}^{up}$ and $\hat{v}^{K}$. The diffusive PDF is light grey, the updraft PDF dark grey, of which the saturated area f^{up} is indicated by the shading. c) The bimodal PDF as projected on the q_t axis.*

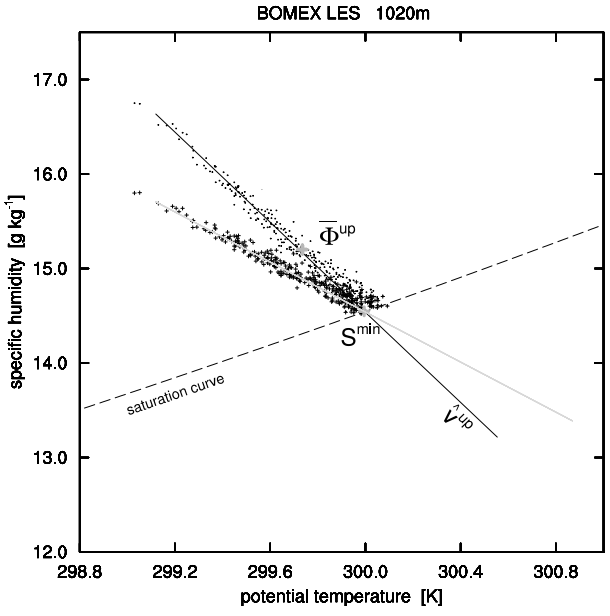

Figure 3: Same as Fig.2, but now only showing the oversaturated $\{\theta_l, q_t\}$ points of the updraft PDF (black dots). The corresponding $\{\theta_l, q_{sat}\}$ points also shown (black plusses), including their linear fit (grey solid line). The updraft PDF mean $\overline{\boldsymbol{\Phi}}^{up}$ and the minimum saturation point $\boldsymbol{S}^{min}$ are both marked (grey thick plus).

on the lateral mixing line between the moist updraft state and the gridbox-mean state, while the diffusive-PDF axis $\hat{v}^{\mathrm{K}}$ is positioned on the zero buoyancy line, reflecting that diffusive motions are only weakly buoyant.

Integrating the total cloud fraction $\mathscr{A}_c$ and total condensate $\overline{l}$ comes down to summation of the contributions by all PDFs weighted by their fractions,

$$\mathscr{A}_c = \mathscr{A}^{\mathrm{up}} f^{\mathrm{up}} + \mathscr{A}^{\mathrm{K}} f^{\mathrm{K}}, \tag{5}$$

$$\overline{l} = \mathscr{A}^{\mathrm{up}} l^{\mathrm{up}} + \mathscr{A}^{\mathrm{K}} l^{\mathrm{K}}, \tag{6}$$

where f is the saturated area fraction and l the condensate on each PDF. As we use fixed (Gaussian) PDF shape functions, these contributions can be written in terms of the *normalized saturation deficit* Q, defined as the distance of the PDF-mean to the saturation curve along the PDF axis normalized by the width of the PDF,

$$f = \mathscr{B}(Q), \qquad Q = \frac{x_{\mathrm{sat}} - \overline{x}}{\sigma_x}, \tag{7}$$

where x is the PDF-axis coordinate, defined as

$$x \equiv \frac{(\boldsymbol{\Phi} - \overline{\boldsymbol{\Phi}}) \cdot \hat{v}}{\|\hat{v}\|}. \tag{8}$$

As a result, the PDF-mean $\overline{x} \equiv 0$ per definition. x_{sat} is the intersection point of the PDF axis with the saturation curve, and $\mathscr{B}$ a Gaussian shape function, expressing the top-fraction of the PDF situated above x_{sat} as a function of Q (precalculated in Table 2, see Appendix A). Intersection point x_{sat} is calculated using a vector-calculus method, as described in Appendix C. Concerning the integration of condensate, the variation of q_{sat} with x in the cloudy part of the PDF is not neglected but is linearized, to properly account for its dependence on temperature. As illustrated by Fig. 3, in cumulus convection temperature varies significantly over the updraft PDF, due to differential latent heat release and lateral mixing rates. Appendix B illustrates that such linearization allows writing

$$l = f \left(\frac{\partial q_t}{\partial x} - \frac{\partial q_{\mathrm{sat}}}{\partial x} \right)_{x_{\mathrm{sat}}} \left(\overline{x}^f - x_{\mathrm{sat}} \right), \tag{9}$$

$$\text{where} \quad \overline{x}^f = \overline{x} + \mathscr{D}(Q)\ \sigma_x, \tag{10}$$

with $\mathscr{D}$ another Gaussian shape function (precalculated in Table 2), expressing the mean of the top fraction f as a function of Q. The gradients with x are estimated at x_{sat}.

3.2 Variance closures

What remains is closure of the variance (or the square width) of each PDF. As described by Lewellen and Yoh (1993) the first and second statistical moments of a bimodal PDF are related as

$$\overline{\phi} = \mathscr{A}^{\mathrm{up}} \overline{\phi}^{\mathrm{up}} + \mathscr{A}^{\mathrm{K}} \overline{\phi}^{\mathrm{K}}, \tag{11}$$

$$\sigma_\phi{}^2 + \overline{\phi}^2 = \mathscr{A}^{\mathrm{up}} \left(\sigma_\phi^{\mathrm{up}2} + \overline{\phi}^{\mathrm{up}2} \right) + \mathscr{A}^{\mathrm{K}} \left(\sigma_\phi^{\mathrm{K}2} + \overline{\phi}^{\mathrm{K}2} \right), \tag{12}$$

where σ_ϕ^{K} and $\sigma_\phi^{\mathrm{up}}$ express perturbations relative to means $\overline{\phi}^{\mathrm{K}}$ and $\overline{\phi}^{\mathrm{up}}$ respectively, as illustrated in Fig.2c. These relations hold for any bimodal PDF, not just binormal ones. The bimodal PDF fractions $\mathscr{A}^{\mathrm{up}}$,$\mathscr{A}^{\mathrm{K}}$ and

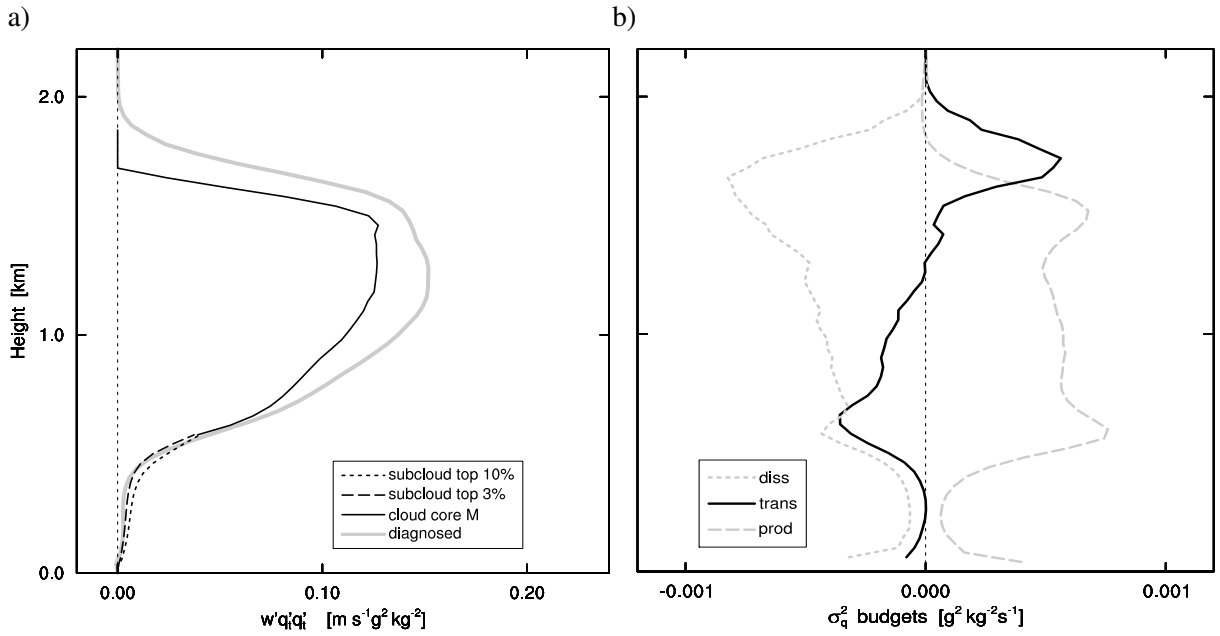

Figure 4: Aspects of the variance budget for the BOMEX case, using hourly averaged LES profiles. a) The variance flux $\overline{w'q_t'q_t'}$, both diagnosed (grey) and parameterized by the mass flux approach (black). Shown are the cloud core (black solid) and two top-percentages of the PDF of vertical velocity in the sub-cloud layer (black dashed and dotted). b) The LES variance budget. The dissipation term is calculated as a residual of the other terms, assuming steady-state.

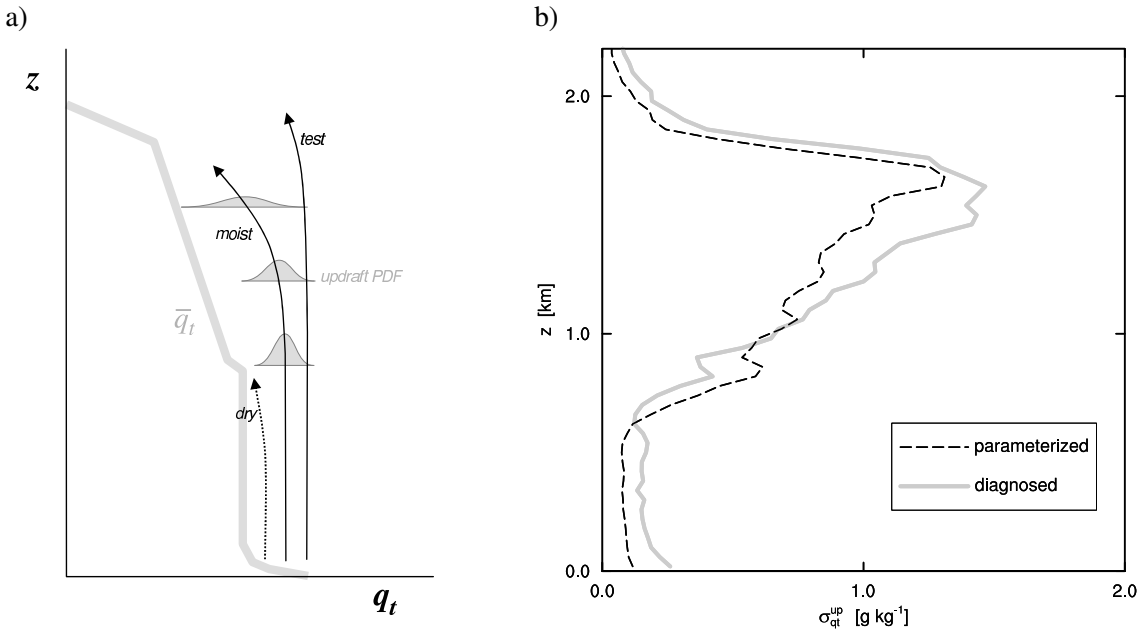

Figure 5: a) Schematic illustration of the increasing width of the updraft PDF with height as implied by the divergence of updraft profiles, through closure (17). b) Offline evaluation in LES of parameterization (17) for the variance among updrafts $\sigma_{q_t}^{up}$, during the BOMEX case.

PDF means $\overline{\phi}^{\mathrm{up}}$,$\overline{\phi}^{\mathrm{K}}$ are provided by the transport model. Remaining closure thus needs to be defined for two of the three variances in (12). We choose here to parameterize the gridbox-mean total variance σ_ϕ^2 and the variance among updrafts $\sigma_\phi^{\mathrm{up}2}$.

Parameter σ_x is the width of each PDF measured along the PDF axis. As the direction of each axis is already determined, the variance of only one conserved variable is required, for which we choose q_t. The prognostic budget of gridbox-mean variance $\sigma_{q_t}^2$ consists of flux-gradient production, transport and dissipation,

$$\frac{\partial {\sigma_{q_t}}^2}{\partial t} = -2\,\overline{w'q_t'}\frac{\partial \overline{q_t}}{\partial z} - \frac{\partial \overline{w'q_t'q_t'}}{\partial z} - \varepsilon, \tag{13}$$

where the horizontal flux components are neglected for simplicity. The storage term is retained, thus making variance a prognostic variable. All three physical processes on the right hand side of (13) are retained and explicitly modeled. The flux in the variance production term in (13) is available from the transport model. The dissipation of variance is parameterized using a relaxation formula,

$$\varepsilon = \frac{{\sigma_{q_t}}^2}{\tau}, \tag{14}$$

where τ is the typical adjustment timescale of dissipation, which is assumed to scale with the turn-over time of the strongest eddies in the PBL,

$$\tau \approx \frac{h}{w_*}. \tag{15}$$

Variance transport is assumed to be similarly dominated by the largest eddies, which motivates the use of a mass flux approach,

$$-\frac{\partial \overline{w'q_t'q_t'}}{\partial z} \approx -\frac{\partial}{\partial z}\sum_{i=1}^{N} M_{ui}\left(q_{t,ui}-\overline{q_t}\right)^2. \tag{16}$$

Figure 4a shows a validation of this approach against LES. The presence of the second q_t' term dominates the vertical structure of variance transport, acting to create strong vertical gradients in $\overline{w'q_t'q_t'}$ at mixed layer top and cloud top, of opposite sign. As a result, variance transport acts to remove variance at cloud base and deposit variance near cloud top. Variance transport by the dry updraft is relatively small, because large humidity excesses only occur when updrafts rise above mixed layer top. Figure 4b shows that transport can not be neglected in the variance budget, particularly near the top of the cumulus cloud layer.

Concerning the parameterization of the variance among updrafts $\sigma_{q_t}^{\mathrm{up}2}$, information on this parameter is contained in the spread among the thermodynamic profiles of two (or more) model updrafts representing different segments of the PDF. For example, a larger difference corresponds to an updraft PDF that is more "stretched", see Fig. 5a. In the DualM framework, the moist updraft ($i = 2$) and a strong non-transporting test updraft ($i = 0, a_{u0} = 0.002$), used to diagnose PBL heights, are available. Positioning the mean of the updraft PDF on the moist updraft profile $q_{t,u2}$ and using precalculated function $\mathscr{D}$ then ties the variance to the two updraft profiles,

$$q_{t,u0} = q_{t,u2} + \mathscr{D}\left(Q^{\mathrm{up}}\right)\sigma_{qt}^{\mathrm{up}}, \tag{17}$$

where Q^{up} is in this case not the saturation deficit, but simply reflects the fixed ratio of test updraft fraction to moist updraft fraction a_{u0}/a_{u2},

$$Q^{up} = \mathscr{B}^{-1}\left(\frac{a_{u0}}{a_{u2}}\right). \tag{18}$$

Here superscript -1 indicates an inverse function. System (17)-(18) enables calculation of $\sigma_{q_t}^{\mathrm{up}}$ as a function of the updraft fractions a_{ui} and means $q_{t,ui}$, using lookup Table 2. In practice, to avoid division by zero, the updraft variance is set to zero for very small moist updraft fractions ($a_{u2} \leq 1.5\ a_{u0}$). The updraft PDF then corresponds to a delta-function, and the normalized saturation deficit in (7) reduces to a Heaviside function.

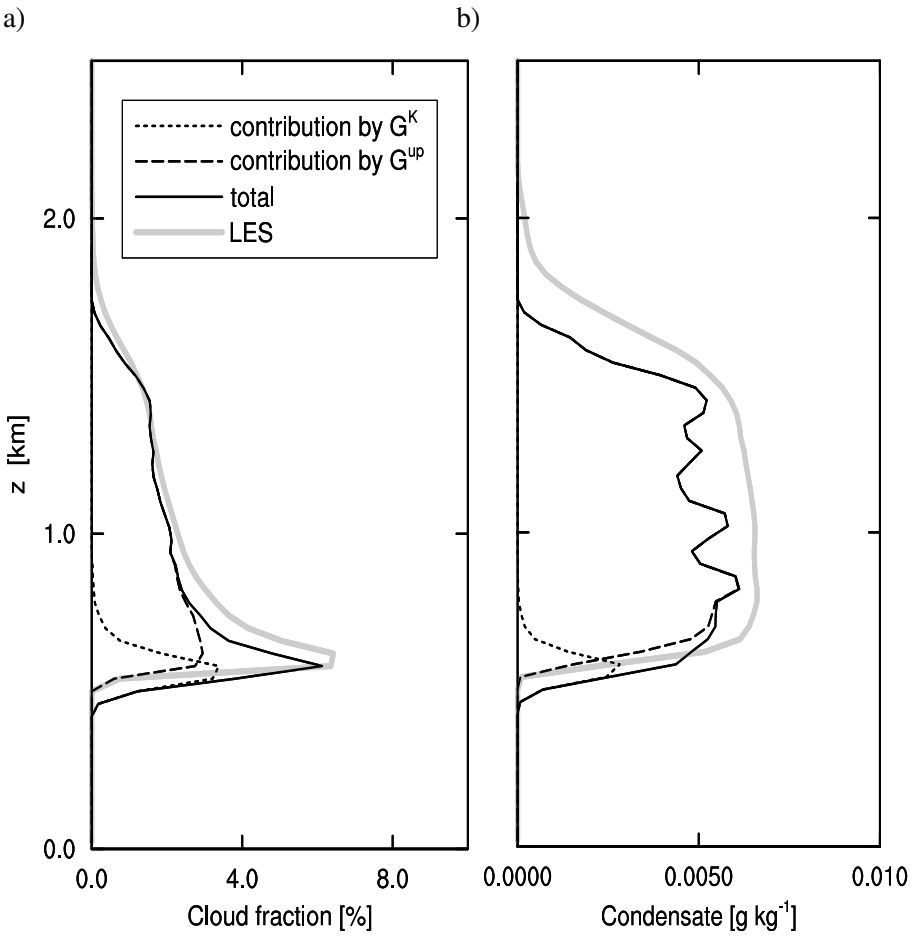

Figure 6: Offline evaluation of the bimodal cloud scheme against LES BOMEX, featuring a) total cloud fraction $\mathscr{A}_c$ and b) total condensate $\overline{l}$. Individual contributions by the updraft PDF and the diffusive PDF are also shown.

Figure 5b shows an offline evaluation of (17)-(18) for LES BOMEX. The parameterization reproduces the increasing updraft variance with height in the cloud layer. The small dents are caused by the use of an instantaneous snapshot 3D field. The more structural differences between the profiles are probably explained by small departures of the real distribution from a pure Gaussian shape, for example featuring a higher skewness. Nevertheless, the parameterization manages to reproduce the bulk of the magnitude of variance among updrafts and its vertical structure.

This technique can be summarized as tying an assumed PDF to a few resolved updrafts to fill in the empty spaces between them. Its evaluation in Fig.5b suggests that resolving only a few updrafts is already sufficient to recreate convective variance structure. This could in theory work as well as resolving many more updrafts to render the PDF. Keeping the number of resolved updrafts as low as possible fits the aim in parameterization to search for the minimum number of free model variables that is required to represent the impact of the unresolved phenomenon.

The variance to be used in the statistical cloud scheme has now become closely tied to the multiple updraft model. For a realistic reproduction of convective cloud fraction and condensate it is therefore prerequisite that the model updrafts reproduce the divergence as observed in Fig. 5b. As described by Neggers et al. (2007), this capability is introduced by the flexible entrainment rate parameterization, featuring an inverse dependendence on vertical velocity. This positive feedback mechanism acts to increase spread among updrafts by enhancing

sensitivity to initial conditions and updraft environment. This will be evaluated in section 4 using single column model simulations.

3.3 Offline evaluation against LES

An offline evaluation of the bimodal framework against LES BOMEX is shown in Fig. 6. All required model-variables ($\overline{\phi}$, ϕ_{u0}, ϕ_{u2}, a_{u2} and σ_{ϕ}) have first been diagnosed in an instantaneous 3D LES field, after which the system of equations is solved. The results show that, given the correct background state, the bimodal framework is capable of reproducing the vertical structure and magnitude of both cloud fraction and condensate. The typical peak in cloud fraction at cumulus cloud base is mainly carried by the diffusive PDF G^{K}. In contrast, in the top half of the cloud layer all cloudiness and condensate is contributed by the updraft PDF G^{up}, due to its residence in the saturated part of the $\{\theta_l, q_t\}$ frame (see also Fig. 2b). This structure of the cloud layer is consistent with observed population statistics of shallow cumulus, with many weak updrafts stopping near cloud base and few stronger updrafts managing to rise further.

4 SCM evaluation

4.1 Setup

All new modules constituting the DualM scheme are implemented into the ECMWF IFS version CY31R1. The scheme in effect replaces the CY31R1 shallow cumulus scheme. Other components of the model physics not addressed in this paper are those as used in CY31R1. The DualM scheme is only applied in the PBL. This means that above the PBL the CY31R1 cloud scheme (Tiedtke 1993) is still active, while within the PBL the new statistical bimodal cloud scheme is applied. This setup completely conserves condensate mass across the PBL boundary. For example, cloud fraction and condensate in the residual PBL is simply picked up and treated by the prognostic Tiedtke scheme, and vice versa.

ATEX Atlantic Trade-wind Experiment *Augstein et al. (1973, 1974)* *Stevens et al. (2001)*
BOMEX Barbados Oceanographic and Meteorological Experiment *Holland and Rasmusson (1973)*, *Nitta and Esbensen (1974)* *Siebesma et al. (2003)*
DYCOMS2 RF01 2nd Dynamics and Chemistry of Marine Stratocumulus field study *Stevens et al. (2003a)*, *Stevens et al. (2003b)* *Stevens et al. (2005)*

Table 1: Summary of prototype PBL cases developed for LES, documenting (in row-order) i) the case acronym, ii) its full name, iii) publications describing the field-experiment and iv) publications describing the LES case setup. The KNMI LES model is described in detail by Cuijpers and Duynkerke (1993).

Single column model (SCM) evaluation is performed for three marine subtropical Trade-wind cases, as developed by GEWEX (Global Energy and Water Experiment) Cloud System Studies (GCSS, Browning 1993) Working Group I on boundary layer clouds. A complete summary of acronyms and references is given in Table

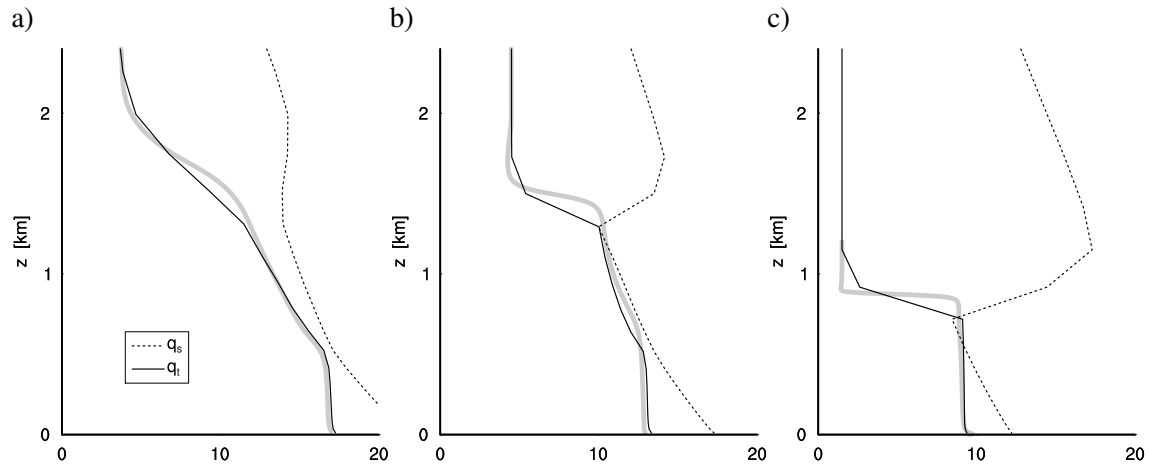

Figure 7: SCM results of the DualM scheme featuring the bimodal cloud scheme, showing mean total specific humidity q_t (solid) and q_{sat} (dotted) for the a) BOMEX, b) ATEX and c) DYCOMS2 case. LES results are plotted in thick grey.

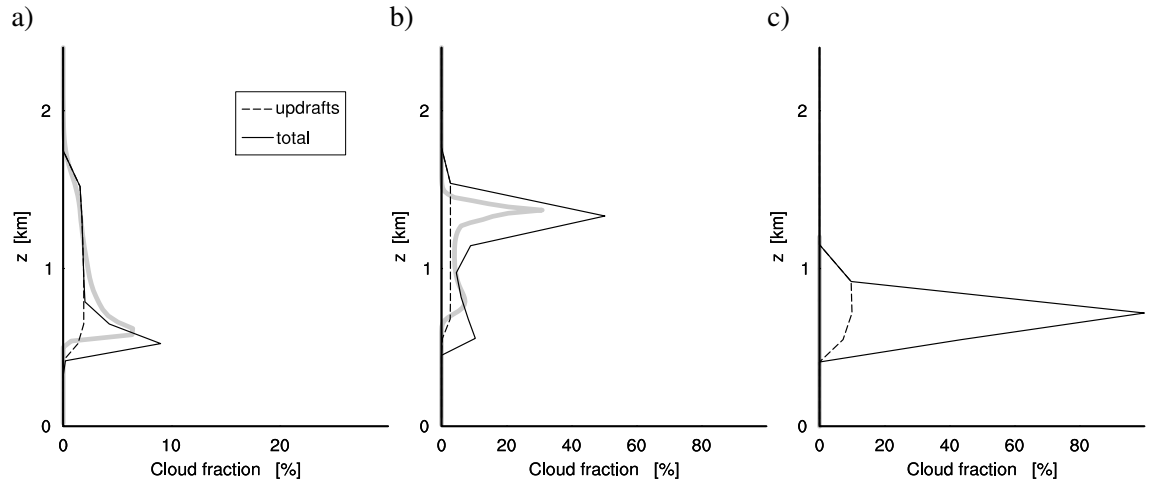

Figure 8: Same as Fig. 7, but now for total cloud fraction $\mathscr{A}_c$. The individual contribution by the updraft PDF is plotted as a dashed line. Note that the plotting range in panel a) is different, for visualization.

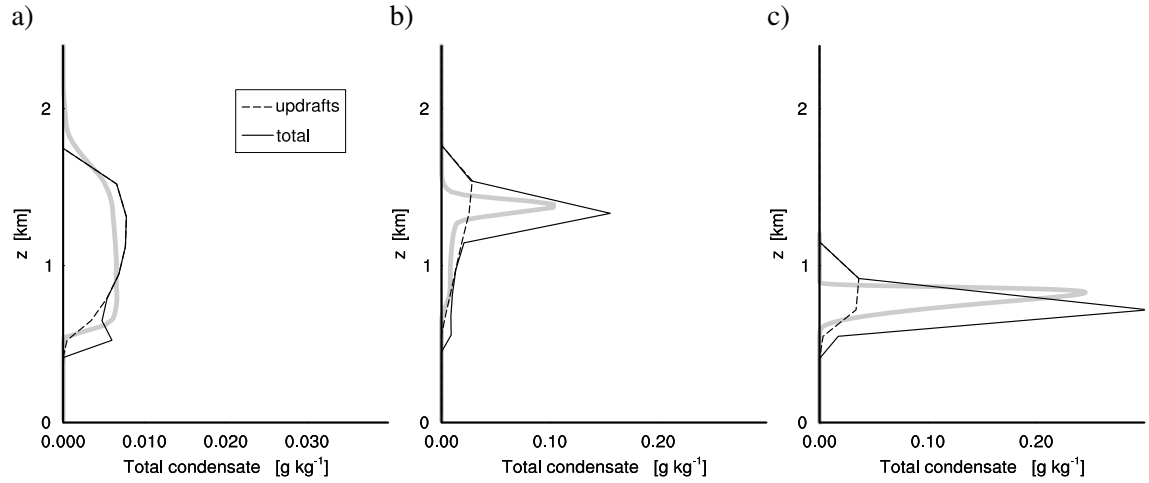

Figure 9: Same as Fig. 8, but now for total condensate $\overline{l}$.

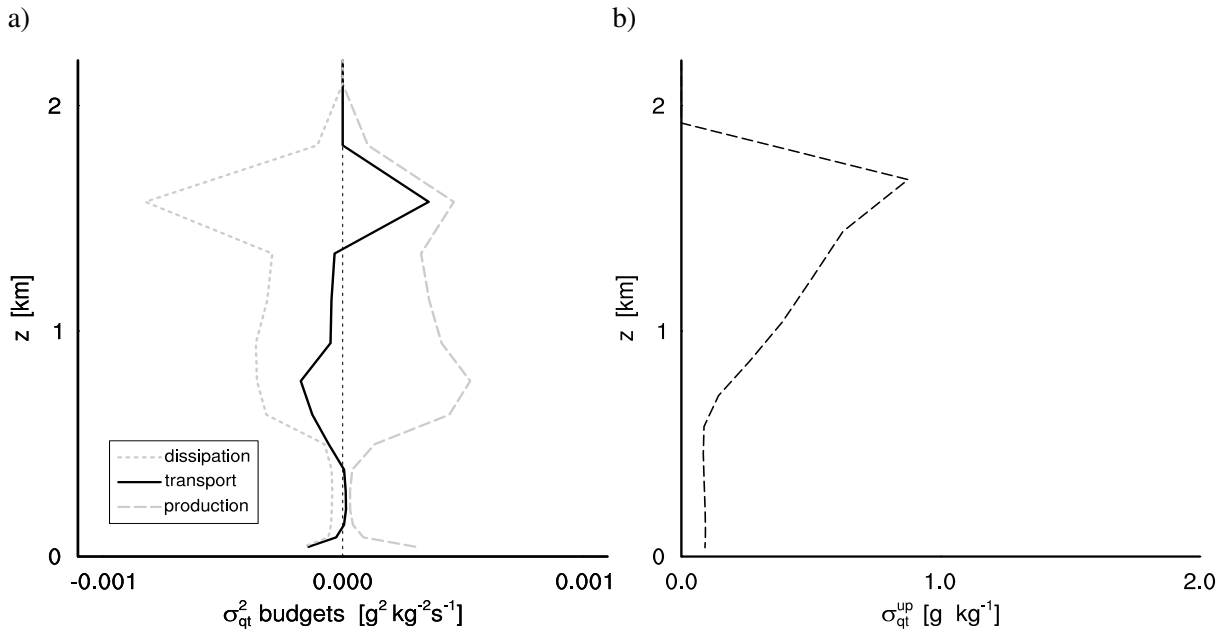

Figure 10: The variance structure of the BOMEX boundary layer as reproduced by the DualM scheme, featuring a) the variance budget terms and b) the square-root of the variance among updrafts ($\sigma^{up}_{q_t}$).

1. The BOMEX case represents shallow cumulus with a relatively small cloud fraction. DYCOMS2 represents stratocumulus with strong subsidence, and ATEX represents the transitional regime, featuring cumuli rising into a capping stratocumulus layer under a strong inversion. LES results are obtained using the code of the Royal Netherlands Meteorological Institute (KNMI), and from the GCSS DIME archive. All SCM simulations are performed at operational CY31R1 vertical resolution, featuring 91 atmospheric levels of which 17 are located in the lowest 2 km. The period of simulation is always four days, to make the time-averages reflect the native equilibrium of the system.

4.2 Case results

Figures 7-9 show the mean and cloudy state as reproduced by the SCM including the bimodal statistical cloud scheme. In general, the vertical structure of PBL mean specific humidity, cloud fraction and cloud condensate is reproduced for all cases. For the BOMEX case, the results of the off-line evaluation against LES (see also Fig.6) carry over to the full SCM simulation, featuring the typical decreasing cloud fraction profile with height and the more or less constant condensate in the cloud layer. For the ATEX case, the typical double-peak profile characteristic of cumulus rising into stratocumulus is reproduced. For the DYCOMS2 case, a total cloud cover of 100% is reproduced (unfortunately no LES data on DYCOMS2 cloud fraction were available to the authors), as well as the relatively high total condensate values typical for this subsidence regime.

The results illustrate that the diffusive PDF acts to represent stratiform cloud layers, while the updraft PDF represents cumuliform clouds. The diffusive PDF acts to increase cloud fraction and condensate automatically when the mean state approaches saturation, for example at shallow cumulus cloud base or near the capping inversion if the latter is strong enough. As discussed by (Neggers et al. 2007), the proximity of mixed layer top to the saturation curve is caused by i) the closure of the moist updraft area fraction, requiring condensation of updrafts, and ii) internal mixed layer transport by the dry updraft, which continuously deposits specific humidity at mixed layer top. The result is a peak in cloud fraction at cloud base, a characteristic feature of

shallow cumulus convection.

The role of the updraft PDF is to create enough cloud fraction and condensate in conditionally unstable cloud layers (see Fig.8a and Fig.9a). In those situations the mean state in the cloud layer can be relatively far from the saturation curve (low relative humidity), and the updraft PDF then forms an isolated mode in the saturated section of conserved variable space. This is the situation visualized schematically in Fig.2b. Another role of the updraft PDF is to create cloudiness and condensate associated with updrafts overshooting a capping stratus layer, visible in both the ATEX and DYCOMS2 case.

The scenario that best demonstrates the benefits of a bimodal, advective-diffusive approach in subgrid cloud representation (and the associated close coupling between the transport and cloud schemes) is the transitional ATEX case. Due to the entrainment efficiency closure at PBL top and the feedback of stability on the vertical structure of cloudy mass flux, the transport model acts to increase humidity flux convergence under stronger inversions, as testified by the steeper $\overline{q_t}$ profile shown in Fig.7b. The resulting high local relative humidity then helps the formation and maintenance of the capping stratocumulus layer, through the diffusive PDF. In turn, the updraft component of EDMF contributes most of the cloud fraction and condensate at lower heights, representing the cumuli that are rising into the stratocumulus layer.

The variance structure of the cumulus topped boundary layer as produced by the DualM scheme is evaluated in Fig. 10. In general, the results of the offline evaluation against LES carry over to the SCM simulations, in which all model components are interactive. Comparing Fig. 10a to Fig. 4b shows that the vertical structure and magnitude of the individual terms in the variance budget are reproduced. Variance production peaks at mixed layer top and the inversion, while transport removes variance from mixed layer top and deposits it at the inversion. Comparing Fig. 10b to Fig. 5b shows that the spread among model updrafts still resembles that in LES.

5 Concluding remarks

In this study the EDMF framework is used to integrate the representation of subgrid diffusive transport, advective transport, and clouds in the PBL. This is achieved by parameterizing all processes in terms of the same reconstructed turbulent distribution, making their representation internally consistent throughout the PBL. Including an additional PDF enhances model complexity, which allows representation of more complex scenarios. The evaluation for a series of prototype scenarios demonstrates that this technique is successful in reproducing the cloudy structure of the major convective PBL regimes, and transitions between those.

An integrated representation of boundary layer clouds and transport, made possible by their unique (turbulent) nature, has some useful consequences. First, successful reproducing one process requires accurate representation of the other. This means that PBL scheme development always involves the whole set of physics, and not just one individual part. Second, the possibility for tuning is significantly reduced. Third, the results show that the enhancement in model complexity that was required for unification does not necessarily lead to model instability. In addition, it allows representation of more complex scenarios, such as the transitional Trade-wind regime.

The applicability of a bimodal decomposition to both cloudiness and transport in the convective boundary layer forms the foundation of this integrated modelling approach. In principle, the EDMF approach can be applied to any process that features the same advection-diffusion bimodality. For example, Kuang and Bretherton (2006) show that bimodal PDFs also exist in deep convective situations, with rising convective towers and capping cirrus outflow layers at the tropopause. Another example is mixed-phase stratocumulus, such as for example observed during M-PACE (Harrington and Verlinde 2004; Verlinde et al. 2005), in which updraft condensate is often found to be mainly in liquid phase while the stratus layer contains most of the ice.

Acknowledgements While affiliated at ECMWF the first author was sponsored by the Atmospheric Radiation Measurement (ARM) Program of the United States Department of Energy (DOE). LES results for the DYCOMS2 RF01 case were obtained from the GCSS Data Integration for Model Evaluation (DIME) archive. We furthermore thank various members of staff at ECMWF for their generous support and feedback during this study.

APPENDIX A

Precalculated functions

Q	$\mathscr{B}(Q)$	$\mathscr{D}(Q)$	Q	$\mathscr{B}(Q)$	$\mathscr{D}(Q)$
3.719	10^{-4}	3.958	1.282	0.1	1.754
3.090	10^{-3}	3.368	0.842	0.2	1.400
2.326	0.01	2.673	0.524	0.3	1.159
2.054	0.02	2.425	0.253	0.4	0.966
1.881	0.03	2.267	0	0.5	0.798
1.751	0.04	2.153	-0.253	0.6	0.644
1.645	0.05	2.062	-0.524	0.7	0.497
1.555	0.06	1.985	-0.842	0.8	0.350
1.476	0.07	1.918	-1.282	0.9	0.195
1.405	0.08	1.859	-3.090	0.999	0.003
1.341	0.09	1.804	$-\infty$	1.	0

Table 2: The area fraction $f = \mathscr{B}(Q)$ and mean $\overline{x}^f = \overline{x} + \mathscr{D}(Q)\sigma_x$ of a top segment (as defined by normalized saturation deficit Q) of the Normal distribution $N(\overline{x} = 0, \sigma_x = 1)$.

APPENDIX B

Linearization of q_{sat}

Figure 3 suggests that the variation of q_{sat} in convective cloud layers is significant. This is explained by the dependence of q_s on temperature, the latter featuring considerable variation in the cloudy tail of the turbulent PDF a result of varying updraft mixing rates and differential latent heat release (Sommeria and Deardorff 1977). We assumed earlier that the joint-PDF lies on a linear axis,

$$q_t(x) \;=\; q_t(x_{sat}) + \left.\frac{\partial q_t}{\partial x}\right|_{x_{sat}} (x - x_{sat})\,. \tag{B1}$$

In combination with the usual local Taylor-expansion of the saturation curve, this implies that $q_{sat}(x)$ can be linearized around x_{sat} as well,

$$q_{sat}(x) \;=\; q_t(x_{sat}) + \left.\frac{\partial q_{sat}}{\partial x}\right|_{x_{sat}} (x - x_{sat})\,. \tag{B2}$$

This allows writing the total condensate at some point x in the cloudy part of the PDF as

$$q_t - q_s \;=\; C\;(x - x_{sat})\,, \tag{B3}$$

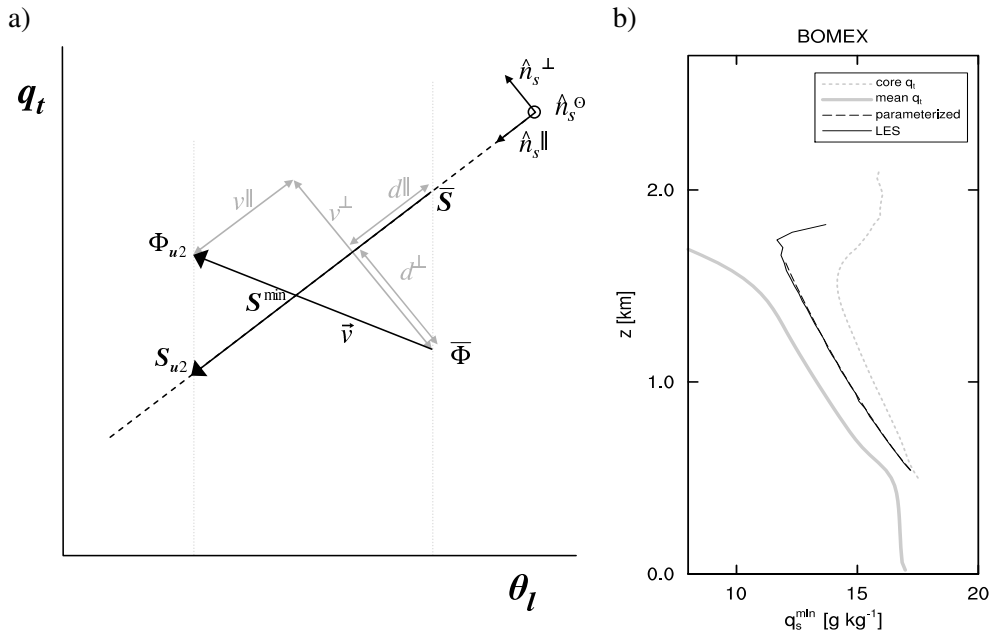

Figure 11: a) Visualization of the vector calculus method for estimating the minimum saturation point $\boldsymbol{S}^{min}$. b) BOMEX vertical profile of q_s^{min}, both parameterized (dashed black) and sampled (solid black) in LES. For reference the total specific humidity of the mean state $\overline{q_t}$ (solid grey) and the cloud core q_t^{co} (dotted grey) are also shown.

where

$$C = \left(\frac{\partial q_t}{\partial x} - \frac{\partial q_{sat}}{\partial x} \right)_{x_{sat}} \tag{B4}$$

is a factor always larger than zero, as the presence of condensate implies that $q_t > q_{sat}$. As oversaturation increases linearly beyond $x_{\rm sat}$, the integral giving PDF-mean condensate l condensate can then be simplified as

$$l = \int_{x_{\rm sat}}^{\infty} (q_t - q_s) P(x) dx = C \int_{x_{\rm sat}}^{\infty} (x - x_{\rm sat}) P(x) dx = f\, C\, (\overline{x}^f - x_{\rm sat}). \tag{B5}$$

APPENDIX C

Saturation deficit in conserved variable space: a vector calculus method

The intersection point $\boldsymbol{S}_{min}$ of a linearized PDF axis and the dry saturation curve is obtained using a vector calculus method, see Fig.11a. We now formulate this method using the updraft PDF as an example (but the principle could apply to any PDF). The axis is defined by the mean state point $\overline{\boldsymbol{\Phi}}$ and the moist updraft point $\boldsymbol{\Phi}_{u2}$,

$$\overline{\boldsymbol{\Phi}} = (\overline{\theta_l}, \overline{q_t}, 0), \tag{C1}$$

$$\boldsymbol{\Phi}_{u2} = (\theta_{l,u2}, q_{t,u2}, 0) \tag{C2}$$

where the third dimension corresponds to the axis perpendicular to the θ_l, q_t plane. The dry saturation curve is linearized as usual, spanned between $\overline{\boldsymbol{S}}$ and $\boldsymbol{S}_{u2}$, defined as

$$\overline{\boldsymbol{S}} = (\overline{\theta_l}, q_s|_{T=\overline{T_l}}, 0), \tag{C3}$$

$$\boldsymbol{S}_{u2} = (\theta_{l,u2}, q_s|_{T=T_{l,u2}}, 0) \tag{C4}$$

A new system is then defined by the following three orthogonal basis vectors,

$$\hat{\mathbf{n}}_s^{\parallel} = \frac{\boldsymbol{S}_{u2} - \overline{\boldsymbol{S}}}{\|\boldsymbol{S}_{u2} - \overline{\boldsymbol{S}}\|} \tag{C5}$$

$$\hat{\mathbf{n}}_s^{\odot} = (0,\ 0,\ 1) \tag{C6}$$

$$\hat{\mathbf{n}}_s^{\perp} = \hat{\mathbf{n}}_s^{\parallel} \times \hat{\mathbf{n}}_s^{\odot} \tag{C7}$$

The linear mixing line is vectorized,

$$\vec{v} = \boldsymbol{\Phi}_{u2} - \overline{\boldsymbol{\Phi}}, \tag{C8}$$

as is the distance of the mean state from the dry saturation curve,

$$\vec{d} = \overline{\boldsymbol{S}} - \overline{\Phi}. \tag{C9}$$

A series of projections is then made onto the new axes $\hat{\mathbf{n}}_s$,

$$v^{\perp} = \frac{\vec{v}\cdot\hat{\mathbf{n}}_s^{\perp}}{\|\hat{\mathbf{n}}_s^{\perp}\|}, \qquad v^{\parallel} = \frac{\vec{v}\cdot\hat{\mathbf{n}}_s^{\parallel}}{\|\hat{\mathbf{n}}_s^{\parallel}\|}, \qquad d^{\perp} = \frac{\vec{d}\cdot\hat{\mathbf{n}}_s^{\perp}}{\|\hat{\mathbf{n}}_s^{\perp}\|}, \qquad d^{\parallel} = \frac{\vec{d}\cdot\hat{\mathbf{n}}_s^{\parallel}}{\|\hat{\mathbf{n}}_s^{\parallel}\|}. \tag{C10}$$

This finally allows expressing the intersection point $\boldsymbol{S}^{min} = (\theta_l^{min}, q_s^{min}, 0)$ in terms of these projections,

$$\boldsymbol{S}^{min} = \overline{\boldsymbol{S}} + \left(d^{\parallel} + v^{\parallel}\frac{d^{\perp}}{v^{\perp}} \right) \hat{\mathbf{n}}_s^{\parallel}. \tag{C11}$$

When $v^{\perp} = 0$ the PDF is either totally saturated or totally unsaturated, in which case the scheme reverts to an all-or-nothing scheme. Figure 11b illustrates that the linearization of both the PDF axes and the saturation curve as applied in this calculus method gives reliable estimates of q_s^{min} throughout the cloud layer. The last remaining operation is then to use (8) to project $\boldsymbol{S}^{min}$ on the PDF axis,

$$x_{sat} = \frac{(\boldsymbol{S}^{min} - \overline{\boldsymbol{\Phi}})\cdot\hat{v}}{\|\hat{v}\|} \tag{C12}$$

for use in the calculation of PDF saturated fraction f and condensate l (see (7) and (9) respectively).

References

Augstein, E., H. Riehl, F. Ostapoff and V. Wagner, 1973: Mass and energy transports in an undistrubed Atlantic trade-wind flow. *Mon. Wea. Rev.*, **101**, 101-111.

Augstein, E., H. Schmidt and V. Wagner, 1974: The vertical structure of the atmospheric planetary boundary layer in undistrubed Trade winds over the Atlantic Ocean. *Bound.-Layer Meteor.*, **6**, 129-150.

Bougeault, P., 1981: Modeling the Trade-wind cumulus boundary layer. Part I: Testing the ensemble cloud relations against numerical data. *J. Atmos. Sci.*, **38**, 2414-2428.

Browning, K. A., 1993: The GEWEX Cloud System Study (GCSS). *Bull. Amer. Meteor. Soc.*, **74**, 387-399.

Cuijpers, J. W. M., and P. G. Duynkerke, 1993: Large-eddy simulation of trade-wind cumulus clouds. *J. Atmos. Sci.*, **50**, 3894-3908.

Golaz, J.-C., V. E. Larson and W. R. Cotton, 2002: A PDF-based model for boundary layer clouds. Part I: method and model description. *J. Atmos. Sci.*, **59**, 3540-3551.

Harrington, J., and J. Verlinde, 2004: Mixed-phase Arctic Clouds Experiment (M-PACE): The ARM scientific overview document. *Report, U.S. Dep. of Energy, Washington, D. C.*, 20 pp.

Holland, J. Z., and E. M. Rasmusson, 1973: Measurement of atmospheric mass, energy and momentum budgets over a 500-kilometer square of tropical ocean. *Mon. Wea. Rev.*, **101**, 44-55.

Holtslag, A. A. M., and C.-H. Moeng, 1991: Eddy diffusivity and countergradient transport in the convective atmospheric boundary layer. *J. Atmos. Sci.*, **48**, 1690-1698.

Houghton J. T., Y. Ding, D. J. Griggs, M. Noguer, P. J. van der Linden, D. Xiaosu, Eds., 2001: *Climate Change 2001: The Scientific Basis.* Cambridge University Press, 944 pp.

Kessler, E., 1969: On the distribution and continuity of water substance in atmopsheric circulation. *Meteorological Monographs*, **10**, Americ.Meteor.Soc., Boston, MA.

Köhler, M., 2005: Improved prediction of boundary layer clouds. *ECMWF Newsletter*, No. **104**, 18-22.

Kuang, Z., and C. S. Bretherton, 2006: A mass-flux scheme view of a high-resolution simulation of a transition from shallow to deep cumulus convection. *J. Atmos. Sci.*, **63**, 1895-1909.

Lappen, C.-L., and D. A. Randall, 2001: Toward a unified parameterization of the boundary layer and moist convection. Part I: A new type of mass-flux model. *J. Atmos. Sci.*, **58**, 2021-2036.

Larson, V. E., R. Wood, P. R. Field, J.-C. Golaz, T. H. Vonder Haar, and W. R. Cotton, 2001: Small-scale and mesoscale variability of scalars in cloudy boundary layers: One-dimensional probability density functions. *J. Atmos. Sci.*, **58**, 1978-1994.

Lewellen, W. S., and S. Yoh, 1993: Binormal model of ensemble partial cloudiness. *J. Atmos. Sci.*, **50**, 1228-1237.

Mellor, G. L., 1977: The Gaussian cloud model relations. *J. Atmos. Sci.*, **34**, 356-358.

Neggers, R. A. J., M. Köhler, and A. Beljaars, 2007: A dual mass flux framework for boundary layer convection. Part I: Transport. *ECMWF ARM Report Series*, **2**, 25pp.

Nitta, T. and S. Esbensen, 1974: Heat and moisture budget analyses using BOMEX data. *Mon. Wea. Rev.*, **102**, 17-28.

Siebesma, A. P., and J. Teixeira, 2000: An advection-diffusion scheme for the convective boundary layer: description and 1D-results. *Proceedings of the 14th Symposium on Boundary Layer and Turbulence of the American Meteorological Society*, 133-140.

Siebesma, A. P., and Co-authors, 2003: A large eddy simulation intercomparison study of shallow cumulus convection. *J. Atmos.Sci.*, **60**, 1201-1219.

Siebesma, A. P., P. M. M. Soares, and J. Teixeira, 2007: A combined eddy diffusivity mass flux approach for parameterizing turbulent transport in the convective boundary layer. *J. Atmos. Sci., in press, March 2007*

Sommeria, G., and J. W. Deardorff, 1977: Subgrid-scale condensation in models of non-precipitating clouds. *J. Atmos. Sci.*, **34**, 344-355.

Stevens, B., and Co-authors, 2001: Simulations of Trade-wind cumuli under a strong inversion. *J. Atmos. Sci.*, **58**, 1870-1891.

Stevens, B., and Co-authors, 2003a: On entrainment in nocturnal marine stratocumulus. *Quart. J. Roy. Meteor. Soc.*, **129**, 3469-3492.

Stevens, B., and Co-authors, 2003b: Dynamics and chemistry of marine stratocumulus – DYCOMS-II. *Bull. Amer. Meteor. Soc.*, **84**, 579-593.

Stevens, B., and Coauthors, 2005: Evaluation of large-eddy simulations via observations of nocturnal marine stratocumulus. *Mon. Wea. Rev.*, **133**, 1443-1462.

Sundqvist, H., 1978: A parameterization scheme for non-convective condensation including prediction of cloud water content. *Q. J. R. Meteorol. Soc.*, **104**, 677-690.

Tiedtke, M., 1993: Representation of clouds in large-scale models. *Mon. Wea. Rev.*, **121**, 3040-3061.

Tompkins, A., and Co-authors, 2004: Moist physical processes in the IFS: Progress and plans. *ECMWF technical memorandum*, 452pp.

Verlinde, J., et al., 2005: Overview of the Mixed-Phase Arctic Cloud Experiment (M-PACE). *Proceedings of the 85th Annual Conference of the Am. Meteorol. Soc., San Diego, Ca.*.

Wyant, M. C., C. S. Bretherton, H. A. Rand, and D. E. Stevens, 1997: Numerical simulations and a conceptual model of the stratocumulus to trade cumulus transition. *J. Atmos. Sci.*, **54**, 168-192.